Materials Today Communications 41 (2024) 110604

Contents lists available at ScienceDirect

Materials Today Communications

journal homepage: www.elsevier.com/locate/mtcomm

Bridging the gap between high-entropy alloys and metallic glasses: Control over disorder and mechanical properties of coatings

Alessandro Troglia [a,1], Cyrian Leriche [a,b], Mike L. van de Poll [a], Christoph Morscher [a], Gert H. ten Brink [c], Bart J. Kooi [c], Bart Weber [a,b], Roland Bliem [a,b,*]

[a] Advanced Research Center for Nanolithography, Science Park 106, 1098 XG Amsterdam, The Netherlands
[b] Van der Waals–Zeeman Institute, Institute of Physics, University of Amsterdam, Science Park 904, 1098 XH Amsterdam, The Netherlands
[c] Zernike Institute for Advanced Materials, University of Groningen, Nijenborgh 4, 9747 AG Groningen, The Netherlands

ARTICLE INFO

Keywords:
Tunable materials
High-entropy alloy
Metallic glass
Thin film
Disorder

ABSTRACT

High-entropy alloys (HEAs) and high-entropy metallic glasses (HEMGs) represent two intensively researched classes of materials with high technological interest for applications as functional coatings with high strength, hardness, toughness, and corrosion resistance. The distinctive structural difference between single-phase crystalline solid solutions for HEAs and liquid-like disorder for HEMGs generates a seemingly insuperable contrast. In this work, we demonstrate that we can deliberately choose between crystalline or glassy properties by introducing structural disorder in HfMoNbTiZr thin films of identical composition. Using pulsed laser deposition (PLD) at different growth conditions, we reproducibly tune the structure of HfMoNbTiZr coatings from crystalline to fully amorphous. We show that the level of disorder has a profound impact on the mechanical properties of the coatings using the hardness derived from nanoindentation measurements as an example. While the hardness of polycrystalline HfMoNbTiZr layers already exceeds the single-phase bulk value, the amorphous HfMoNbTiZr is even clearly harder, demonstrating a distinctive improvement with introducing disorder. Our findings bridge the two seemingly different concepts of HEAs and HEMGs and demonstrate that structural disorder is not a given material property. Instead, disorder can serve as a useful design parameter for customizing the properties of functional coatings.

1. Introduction

The properties of materials are inextricably linked to their level of disorder. Structural disorder in glassy materials [1–7] and defect-induced conductivity [8–10] are classic examples of the dominant role of disorder. More recently, novel and unusual properties in alloys with multiple principal elements [11–14] have attracted the attention of the materials science community [15–18]. In these so-called high-entropy alloys (HEAs), configurational disorder on a single-phase crystalline lattice yields properties beyond the superposition of the constituent elements [12,13]. Research on high-entropy materials has become a hot topic, also extending to the realm of thin films to meet the persistent demand for coatings with ever-improving properties such as strength, hardness, toughness, and wear resistance [19–21]. While the HEAs for coatings are often selected based on the remarkable features of bulk HEAs, the step to thin films provides access to additional degrees of freedom to optimize material properties. Here, we demonstrate that deliberately introducing structural disorder without modifying the composition can further enhance the already promising properties of HEAs.

High-entropy alloy thin films are a new class of coatings, aimed at exceeding the performance of conventional alloys in challenging environments, where for instance a combination of high stability and hardness at elevated temperatures is required [22]. Indeed, reports on high-entropy alloy thin films confirm their outstanding performance as coatings with high thermal and chemical stability at elevated temperatures, excellent strength and hardness, superior resistance to irradiation, wear, fatigue, corrosion, and oxidation [19–21,23]. In particular, HEA thin films based on refractory metals like Nb, Mo, Ta, and W have attracted considerable interest thanks to their excellent mechanical properties such as high strength and toughness, and thermal stability owing to their high melting point [22,24–27]. Among the vast class of refractory HEAs, HfMoNbTiZr has been selected for the present study of high-entropy alloy thin films, based on the remarkable

* Corresponding author at: Advanced Research Center for Nanolithography, Science Park 106, 1098 XG Amsterdam, The Netherlands.
E-mail address: r.bliem@arcnl.nl (R. Bliem).
[1] Present address: TNO, Stieltjesweg 1, 2628 CK Delft, The Netherlands.

https://doi.org/10.1016/j.mtcomm.2024.110604
Received 21 September 2024; Accepted 2 October 2024
Available online 5 October 2024
2352-4928/© 2024 The Authors. Published by Elsevier Ltd. This is an open access article under the CC BY license (http://creativecommons.org/licenses/by/4.0/).

properties reported for HfNbTiZr-based bulk alloys, including solid-solution strengthening, strain hardening, homogeneous deformation, and structural stability, as well as properties of general interest such as high hydrogen storage capacity and superconductivity [28–31].

Finding the ideal functional coating is well known to require more optimization than just the selection of elements, exemplified by the effects of various heat treatments on material properties [32]. The role of disorder and imperfections is also essential for the application of materials. Vacancies, grain boundaries, or surface roughness, for example, are known to strongly affect the physical, chemical, and electrical properties of polycrystalline alloys [33,34]. Even stronger effects can be achieved by selecting materials that prefer to form metallic glasses, which have been shown to exhibit different mechanical properties, such as hardness, ductility, and deformation behavior, also as thin films [35]. In the case of high-entropy materials, the beneficial effects of disorder have led to the emergence of the class of high-entropy metallic glasses (HEMGs), which have shown excellent mechanical and electrical properties, structural stability, and resistance to annealing and irradiation [36–38]. Reports of remarkably high hardness in HEMGs [36,39–42] are attributed to their fully disordered structure, characterized by the absence of grain boundaries, point defects and long-range order. While HEMGs and HEAs are typically characterized by different compositions, favoring either amorphicity or crystallinity, thin films offer additional structural versatility via the tuning of growth parameters. Also for binary alloys, it is possible to modify the growth conditions such that layers close to or far from equilibrium can be achieved [43]. A recent example using PLD of CuZr demonstrates the significant effect of structural disorder on electronic, optical, and surface chemical properties of alloy layers [44]. Deliberately introducing structural disorder via off-equilibrium layer growth eradicates the co-dependence of structure and stoichiometry, opening up new pathways to customize existing materials for new applications. Building a bridge between HEAs and their glassy counterparts will add versatility to this highly promising class of materials, for example allowing for the application of a single HEA as hard coating and as mechanically compliant film.

Here, we demonstrate that the hardness of the high-entropy alloy HfMoNbTiZr can be improved by deliberately introducing structural disorder to this material, which typically forms a single-phase crystalline structure [29,31]. By appropriately tuning the substrate temperature during PLD, different levels of structural disorder are obtained, ranging from fully amorphous to polycrystalline, without variation of the average chemical composition. The resulting amorphous HfMoNbTiZr thin films clearly outperform their crystalline counterpart in hardness. Our results thus establish structural disorder as an effective parameter to tune the properties of high-entropy alloy thin films, merging the concepts of HEAs and HEMGs for versatile functional coatings.

2. Methods

2.1. Sample preparation

HfMoNbTiZr thin films were deposited onto 5×5 mm^2 $Al_2O_3(0001)$ substrates (Siegert Wafer GmbH) via pulsed laser deposition (PLD) using a KrF excimer laser (λ = 248 nm, 20 ns pulse duration) with a typical energy density of 10.5–11.0 J/cm^2 and laser repetition rate of 10 Hz. Sapphire substrates were chosen for their thermal stability, minimal intermixing with the substrate, high hardness, and availability of high-quality stoichiometric samples. The substrates were cleaned prior to deposition with sequential ultrasonic baths of acetone and isopropanol. A custom-made equiatomic HfMoNbTiZr target was used for the deposition process. The target was synthetized by arc-melting using powders or pieces of high-purity Hf (99.90%), Mo (99.95%), Nb (99.99%), Ti (99.99%), and Zr (99.95%). During the fabrication process, the target was re-melted more than 10 times after turning and rotating to ensure homogeneity. The base pressure of the PLD system was better than 5.0×10^{-10} mbar at room temperature and below 10^{-7} mbar at the maximum growth temperature of 900 °C. All the depositions were performed in 4.0×10^{-2} mbar Ar (purity 6.0) background pressure. During all depositions, the chamber pressure is dominated by the high pressure of Ar. Contaminants in the Ar gas and the gas lines (evacuated using a turbomolecular pump) are expected to lead to a level of contamination $\approx 10^{-7}$ mbar. An infrared laser heater (λ = 980 nm) was used to heat the substrate while the temperature was monitored with a pyrometer. The thickness of the films ranged between 20 nm and 100 nm. These thicknesses were determined from the amount of material deposited per laser shot, estimated from a room-temperature growth calibration using atomic force microscopy (Bruker Dimension Icon microscope operated in tapping mode in air). For this measurement, a sharp step of the full film thickness was prepared by locally applying a droplet of soluble photoresist material before PLD growth, and dissolving it in acetone after deposition. The room-temperature growth rate calculated from this step height is used as estimate for all layer thicknesses. The uncertainty based on differences in density of layers grown at different temperatures is expected to be small and all metals in HfMoNbTiZr have negligible vapor pressures at the maximum temperature of 900 °C. The elemental composition of the custom-made HEA target and deposited HEA thin films was measured by means of energy-dispersive x-ray spectroscopy (EDX) using a FEI Verios 460 SEM-EDX system equipped with a Schottky field electron gun and an Oxford Xmax 80 detector. SEM images of the surface morphology were acquired using the same setup, with an electron energy of 10 keV and beam current of 100 pA.

2.2. X-ray diffraction

The structural properties of HEA thin films grown at different conditions were investigated *ex situ* by means of grazing incidence x-ray diffraction (GI-XRD), minimizing the signal from the substrate. For each set of growth parameters we report, the structural data was reproduced on at least three different samples. The GI-XRD investigation was performed using a Bruker D8 QUEST diffractometer system equipped with an Incoatec IμS 3.0 CuKα x-ray source (λ = 1.5406 Å) and a PHOTON II Charge-integrating Pixel Array Detector (CPAD). The diffractograms were obtained by integrating over lines of constant 2θ angle on the 2D detector using the Bruker APEX4 software. The GI-XRD angle was optimized for each sample to minimize the peak of the substrate, because the diffractometer is not optimized for positioning samples in grazing-incidence geometry with calibrated angles. The integration areas are highlighted in the 2D diffraction patterns by light blue lines. Additional bright, sharp diffraction peaks attributed to crystalline melt-ejected droplets during deposition [44] have been removed in Fig. 1 for clarity (see Figure S1 of the Supporting Information for the raw data and additional information).

2.3. Transmission electron microscopy (TEM)

A JEOL 2010 operating at 200 kV (and equipped with a LaB_6 electron source) was used to record selected area electron diffraction (SAED) patterns and bright-field TEM images with relatively small objective aperture to generate strong scattering contrast to differentiate between amorphous and (nano)crystalline structures. TEM samples were produced by depositing the HEA films directly onto 20 nm thick silicon-nitride membranes and then directly capping these films with a 10 nm amorphous Si layer. For comparison, TEM samples without capping layer were produced and analyzed. The thickness of all TEM samples was approximately 20 nm.

2.4. X-ray photoelectron spectroscopy (XPS)

XPS measurements were performed in an ultra-high vacuum (UHV) setup (base pressure below 1.0×10^{-9} mbar) equipped with a Scienta Omicron R4000 HiPP-3 analyzer (swift acceleration mode, 1 mm entrance slit) and a monochromatic Al-Kα x-ray source (1486.6 eV). The HEA thin films were investigated immediately after deposition to infer the chemical composition and overall purity of the surface: the samples were transferred from the PLD growth chamber to the XPS analysis chamber via an UHV transfer system to prevent contamination due to air exposure.

2.5. Hardness measurements

The hardness of the HfMoNbTiZr thin films and the bulk PLD target was determined via nanoindentation measurements performed using a Femtotools FT-I04 system equipped with a Berkovich diamond tip (radius ≈200 nm) and FT S-20000 bi-axial MEMS force sensors. The indentations were performed in 'continuous stiffness measurement' (CSM) mode [45] (200 Hz frequency, 2 nm amplitude, loading rate 10 nm/s), providing continuous results as a function of penetration depth. Before each set of measurements, the nanoindentation tip was calibrated on a fused silica lens (Thorlabs) reference sample to exclude the effect of tip shape changes between measurements. To minimize the contribution of the Al_2O_3(0001) substrate, films of a thickness of at least 100 nm were used and the indenter maximum penetration depth was set to 180 nm. The hardness values were then extracted by averaging more than 30 measurements performed on different locations distanced several microns from each other. The analysis of the individual indentation curves reveals a random variation between indentations on the same sample, in line with a stable shape of the indenter tip. For the bulk HEA target, the maximum penetration depth was set to 1.2 μm to minimize the contribution of the much higher surface roughness. Effects of pile-up and sink-in during the measurements were taken into account by calibration of the tip area function. If the ratio of the total plastic deformation to the maximal penetration depth is close to or smaller than 0.7, pile-up is expected to be of minimal influence in the measurements [45]. For our experiments this ratio is close to 0.65, both for the crystalline and amorphous samples.

3. Results

To paint a comprehensive picture of HfMoNbTiZr thin films, we connect the growth parameters to measurements of the structure, composition, topography, and hardness of the layers. The structural investigation was performed by means of GI-XRD with a 2D detector. Fig. 1.a provides an overview of the temperature-dependent diffractograms obtained from samples grown at substrate temperatures ranging from room temperature (RT) up to 900 °C. The diffraction pattern of the HEA film grown at RT corresponds to the one expected from amorphous structures [44,46,47], exhibiting two broad and weak peaks (commonly referred to as amorphous halos) centered at approximately 37° and 63°, with a full width at half maximum (FWHM) of 5.5° and 10.5°, respectively. These peaks are also characteristic of the diffractogram of the sample grown at 700 °C, although a clear narrowing is discernible (FWHM reduces to approximately 3.6° and 7.5°). The broad, low-intensity peak at 54° is ascribed to an attenuated signal stemming from the Al_2O_3 substrate, visible as weak spots at the edges of the integration area (light blue lines) in the 2D diffraction pattern. Upon increasing the temperature to 800 °C, sharp additional peaks around 38°, 52° and 57° are observed, indicating the formation of crystalline ordered phases [44,47], while the amorphous halos further narrow and shift towards higher diffraction angles. On the other hand, the diffraction pattern of the HEA film deposited at 900 °C displays very different features, dominated by well-defined sharp reflections at positions of 28°, 29°, 38°, 41°, 51°, 58°, and 68°. The bright spots at well-defined angles on the 2D-detector image demonstrate a high orientational preference (Fig. 1.e). Additionally, the amorphous halos are no longer observed. As a comparison, GI-XRD measurements were also performed on the HEA bulk target used for the PLD depositions (blue curve in Fig. 1.a), which displays sharp reflections produced by the Debye–Scherrer rings at positions 38°, 54°, 68° and 80°, in good agreement with the expected single-phase body-centered cubic (BCC) crystal structure with a = 3.36 Å reported for HfMoNbTiZr in literature [29].

To assess whether the crystalline nature of the Al_2O_3(0001) substrate is critical for the onset of crystallinity of the layer, a HEA thin film was deposited onto an amorphous substrate, Si(100) coated with a 100 nm thick amorphous Si_3N_4 film, at 900 °C. The deposition onto an amorphous layer is expected to remove any substrate-induced orientational preference. Indeed, no clear orientational preference is observed for the HEA film deposited onto amorphous Si_3N_4 (Fig. 1.a and .f). The 2D diffraction pattern is dominated by continuous diffraction rings characteristic for randomly oriented polycrystalline layers. The two broad, localized spots detected at approximately 45°and 85°are ascribed to the underlying Si(100) substrate. The integrated diffractogram of the HEA film deposited onto Si_3N_4 is similar to the one on Al_2O_3(0001): sharp peaks associated with crystalline phases are detected, while the amorphous halos are not observed. However, several additional peaks at lower diffraction angles and a splitting of the main peak at 38° are observed.

High-resolution structural characterization in real and reciprocal space has been performed by means of transmission electron microscopy and diffraction of selected HEA thin films. Fig. 2 shows representative TEM images of HEA thin films deposited at RT (a) and at 700 °C (d), together with the corresponding SAED pattern (b, e). No crystallites or ordered regions are discernible in the real-space images for both growth temperatures (RT and 700 °C). The residual contrast in the images of Fig. 2.a and .d is attributed to local variations in density or thickness of the layers in combination with the fact that the images were taken at relatively large defocus. The diffraction pattern of the HEA film grown at RT reported in Fig. 2.b exhibits only two broad and featureless rings of homogeneous intensity (Fig. 2.c), which is characteristic for an amorphous layer. Also for the HEA film grown at 700 °C, broad and liquid-like diffraction features dominate the pattern, as shown in Fig. 2.e. However, an additional weak but narrower and discontinuous ring is visible close to the second broad one (Fig. 2.f), indicating the presence of a minority phase of extremely small crystallites. Based on the absence of more distinct features in the diffraction pattern and of a clear signature of particles in TEM images, these particles are estimated to be approximately 1–2 nm in diameter, embedded in the amorphous matrix.

The microstructure of HfMoNbTiZr layers at 700 °C and above is illustrated by the TEM and SEM images in Fig. 3. While the substrate temperature during growth was 700 °C for the sample in Fig. 3.a, the local temperature was temporarily increased by the arrival of a large droplet of hot melt, ejected from the PLD target. This typical synthesis artifact of PLD generates a temperature gradient in the (amorphous) film, mimicking the effect of a short annealing step. This local heating is not fully equivalent to a higher growth temperature, but provides qualitative insight into the material's preferred microstructural evolution at elevated temperature in a single image. Fig. 3.a–b shows TEM results focused on a region close to an extraordinarily large melt droplet (dark circular feature in Fig. 3.a with a diameter of approximately 10 μm), which was ejected during PLD growth and landed at the surface with high temperature. Two distinct regions characterized by different morphologies are clearly discernible in the TEM image of Fig. 3.a, with the area in the proximity of the droplet exhibiting larger contrast variations and clear signs of granularity. A zoomed-in TEM image reported in Fig. 3.b corresponding to the black dashed square in panel (a) reveals a gradual transition towards increasing crystalline order as one approaches the immediate vicinity of the droplet. With

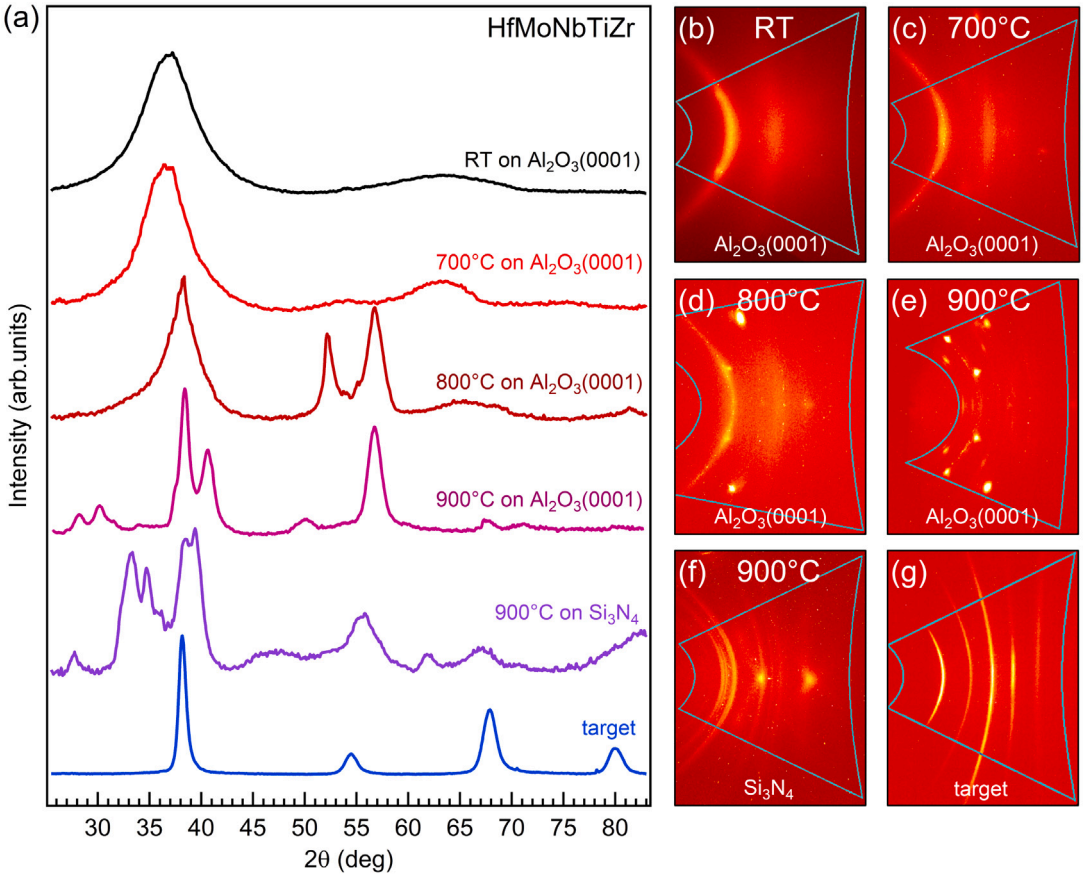

Fig. 1. (a) GI-XRD results of HfMoNbTiZr thin films deposited onto Al_2O_3(0001) at different substrate temperatures. The diffractograms have been normalized by height. HEA thin films deposited at RT (black curve) and at 700 °C (red curve) display an amorphous structure. After increasing the temperature to 800 °C (dark red curve), sharp crystalline diffraction peaks appear, and dominate the diffractograms of the samples grown at 900 °C onto Al_2O_3(0001) (purple curve), and at 900 °C onto Si_3N_4 (violet curve). As a comparison, the GI-XRD pattern of the HEA target used for the deposition is also reported (blue curve), displaying a single-phase BCC crystal structure [29]. Sharp diffraction peaks attributed to melt-ejected droplets during deposition have been removed (see Figure S1 of the Supporting Information). (b–g) Corresponding 2D detector images: the integration of the area marked with a light-blue solid line allowed to extract the diffractograms reported in (a). The 2D diffraction patterns of (b–c) are dominated by broad continuous rings, indicating an amorphous structure. In contrast, sharp diffraction spots at well-defined angles are visible in (d–e), indicating preferential orientation of crystallites. (For interpretation of the references to color in this figure legend, the reader is referred to the web version of this article.)

decreasing distance to the droplet, the size and density of crystallites (dark and bright spots) increase up to patches of comparable brightness of approximately 100 nm in size. Smaller but clear crystallites are observed even several micrometers away from the droplet, therefore suggesting a high level of crystallinity over extended areas close to the droplet. The SAED pattern of Fig. 3.c (corresponding to the area in Fig. 3.b) shows several continuous and well-defined diffraction rings in the vicinity of the reciprocal distance expected for the original BCC-type crystal structure of the HEA (marked with dashed red circles), as expected for a polycrystalline film. An additional distribution of bright diffraction spots is visible around the rings, corresponding to XRD diffraction angles varying from approximately 32° to 42°. A direct comparison between GI-XRD of the HEA grown at 900 °C onto Si_3N_4 and a TEM SAED line profile of Fig. 3.c is reported in Fig. 3.d. The SAED line profile shows similarities with the GI-XRD diffractogram, with the appearance of additional diffraction peaks with respect to the original BCC-type crystal structure. The surface morphology and microstructure of 100 nm thick HfMoNbTiZr layers grown on Al_2O_3(0001) at RT and 900 °C is shown in Fig. 3.e and .f, respectively. The sample grown at RT shows connected patches with soft edges and diffuse corners, attributed to the oxide overlayer forming upon air exposure. Deposition at 900 °C, on the other hand, results in grains separated by gaps, indicative of columnar growth.

For the comparison of amorphous and polycrystalline layers of the same alloy, it is important to ensure that differences between the layers are not dominated by variations in stoichiometry transfer during thin-film growth. The elemental compositions of the HEA films and the bulk PLD target, as measured by EDX are reported in Table 1. The target used for PLD exhibits a close-to-equimolar chemical composition, showing a minor depletion (≈2.5 at.%) in Nb content and slight enrichment in Ti content, while the values of Hf, Mo and Zr content are compatible with the nominal ones within the EDX experimental error of ±1 at.%. On the other hand, the HEA thin films exhibit an elemental composition with clear differences as compared to the bulk target, with approximately 4 at.% enrichment in Mo and Zr, and 5 at.% depletion in Hf and Ti. The difference in elemental composition between target and thin films is ascribed to resputtering effects and scattering of the ablated material with the Ar background, which are common phenomena occurring in PLD of metallic thin films [44,48,49]. The HEA thin films deposited onto sapphire substrates at RT and high temperature (800 °C) exhibit the same elemental composition within the experimental error of EDX. Typical scanning electron microscopy (SEM) images of the HfMoNbTiZr HEA thin films are reported in Figure S2 of the Supporting Information and show a smooth and homogeneous surface morphology. As a result of melt-ejection of droplets during laser ablation, a low density of particles with diameters ranging from tens of nanometers up to a few micrometers are deposited onto the surface.

The surface composition and impurity content were investigated using x-ray photoelectron spectroscopy. Figure S3 of the Supporting Information shows an XPS survey spectrum of an as-grown HEA thin film (thickness approximately 100 nm) measured after deposition at

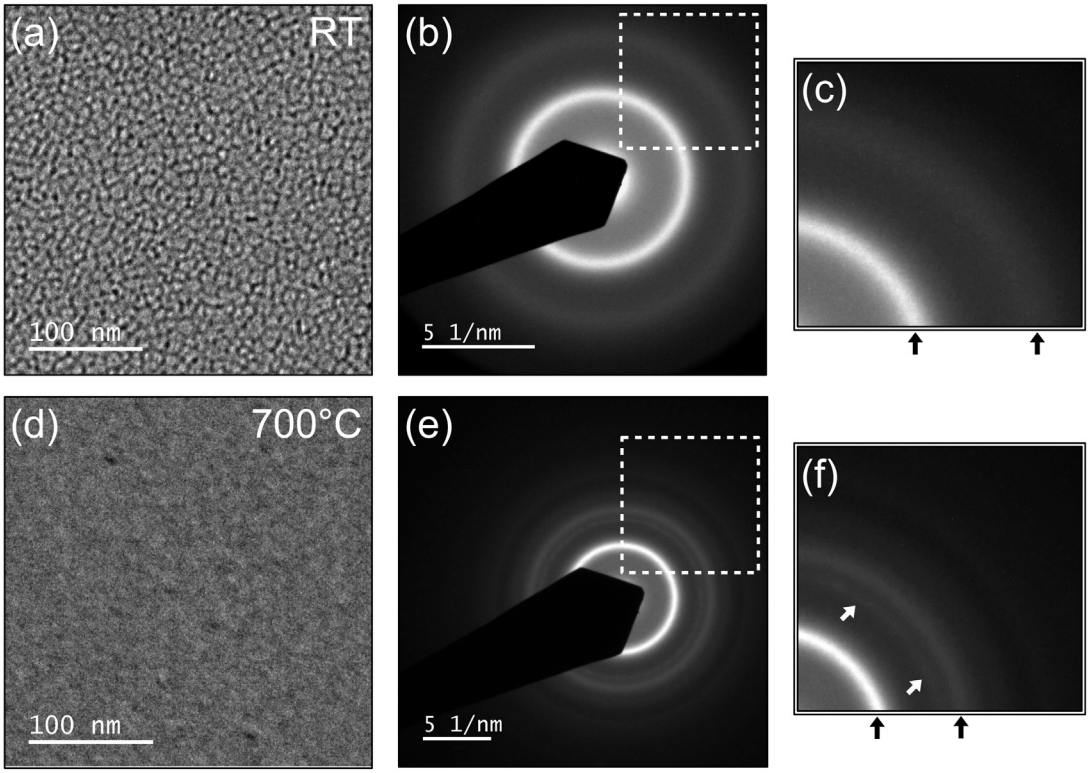

Fig. 2. TEM analysis of HfMoNbTiZr thin films (approximately 20 nm thick) deposited onto Si_3N_4 TEM windows and capped with an amorphous Si layer (approximately 10 nm thick). Top: TEM image of an as-grown HEA thin film deposited at room temperature (a), and corresponding SAED (b). (c) Zoomed-in panel in correspondence of the white dashed square in (b): only two broad continuous rings are visible (black arrows). Bottom: TEM image of a HEA thin film deposited at 700 °C (d), and corresponding SAED pattern (e). (f) Zoomed-in panel in correspondence of the white dashed square in (e): an additional weak and discontinuous ring is visible (white arrows).

Table 1
Elemental composition (in at.% as measured by EDX) of HfMoNbTiZr thin films deposited at RT and 800 °C, compared with the HEA PLD target. The thickness of both films was approximately 100 nm. The EDX experimental error is estimated at ±1 at.%.

	Hf	Mo	Nb	Ti	Zr
Nominal	20.0	20.0	20.0	20.0	20.0
HEA-target	20.5	19.3	17.5	22.4	20.3
HEA-RT	15.4	23.7	19.2	17.6	24.1
HEA-800 °C	14.1	24.8	19.1	18.0	24.0

RT, and transferred to the analysis tool in UHV without air exposure. For comparison, also a survey spectrum after growth at 900 °C and UHV transfer and air exposure of a sample grown at RT are shown. After RT growth in vacuum, the XPS survey exhibits only the core level peaks assigned to Hf, Mo, Nb, Ti and Zr, with minor traces of oxygen. The detection of small traces of oxygen is ascribed to the interaction of highly reactive elements such as Zr and Hf with residual water in the deposition and measurement UHV chambers. Upon air exposure, the deposition of carbon and the oxidation of all metals in the surface region are observed. The sample grown at 900 °C shows a substantially higher oxygen content in the surface region (≈43 at.%) after cooldown and transfer in ultra-high vacuum. This is attributed to enrichment of Hf and Zr at the surface to form HfO_2 and ZrO_2. EDX measurements of HfMoNbTiZr/Si_3N_4 samples grown at RT and at 900 °C, however, show very little difference in oxygen content (28% for RT versus 26% for 900 °C, acquired at low beam voltage, increasing the sensitivity for light elements), demonstrating that the increased oxidation for the high-temperature samples is purely a surface effect.

To quantify the interplay between thin film structure and mechanical performance, we investigated the hardness of the HEA thin films using nanoindentation in continuous stiffness measurement mode. Fig. 4.a shows the measured depth-dependent hardness data of fully amorphous (blue curve, grown at room temperature) and crystalline (red curve, grown at 900 °C) HfMoNbTiZr HEA films on Al_2O_3(0001), averaged over 30 independent indentation measurements. Owing to the small film thickness, the hardness value on the *y* axis should be interpreted as the convolution of the HfMoNbTiZr films and the Al_2O_3(0001) substrates. An initial rise in the measured hardness is observed in the first 30 nm of indentation depth, which is typically caused by an inaccuracy of the nanoscale geometry description of the diamond indenter (Berkovich tip, 3-sided pyramid) and sample (smooth flat). This leads to a varying definition of the contact area function with penetration depth, which forms the basis of the Oliver-Pharr model used in this measurement [45]. At indentation depths beyond 30 nm a clear difference in the hardness signal is measured for amorphous HfMoNbTiZr/Al_2O_3(0001) and crystalline HfMoNbTiZr/Al_2O_3(0001). This difference decreases as the indentation depth increases and the mechanical properties of the underlying Al_2O_3(0001) start dominating the measurement. We therefore interpret the plateau region between approximately 30 nm and 50 nm (inset of Fig. 4.a) as indicative of a *minimal* contrast in hardness. The absolute hardness values, however, should be regarded as upper limits of the film hardness as the measurement in this regime is influenced by the harder substrate. As a comparison, nanoindentation was also performed on the bulk HEA PLD target and the Al_2O_3(0001) substrate, respectively; the results are displayed in Figure S4. The HEA target (Figure S4.a) displays a substantially lower hardness compared to the thin films, exhibiting a value of H = 4.7 ± 0.6 GPa. The measurement of the target displays a high standard deviation of the hardness and reduced modulus signals at low indentation depth (below 500 nm). This can be attributed to the high roughness of the surface, adding uncertainty to the measured value. The Al_2O_3(0001) substrate measurement (Figure S4.c) shows a hardness value of 28 ± 1 GPa. We observe in Fig. 4.a that the hardness curves reasonably tend to this value as the penetration depth increases.

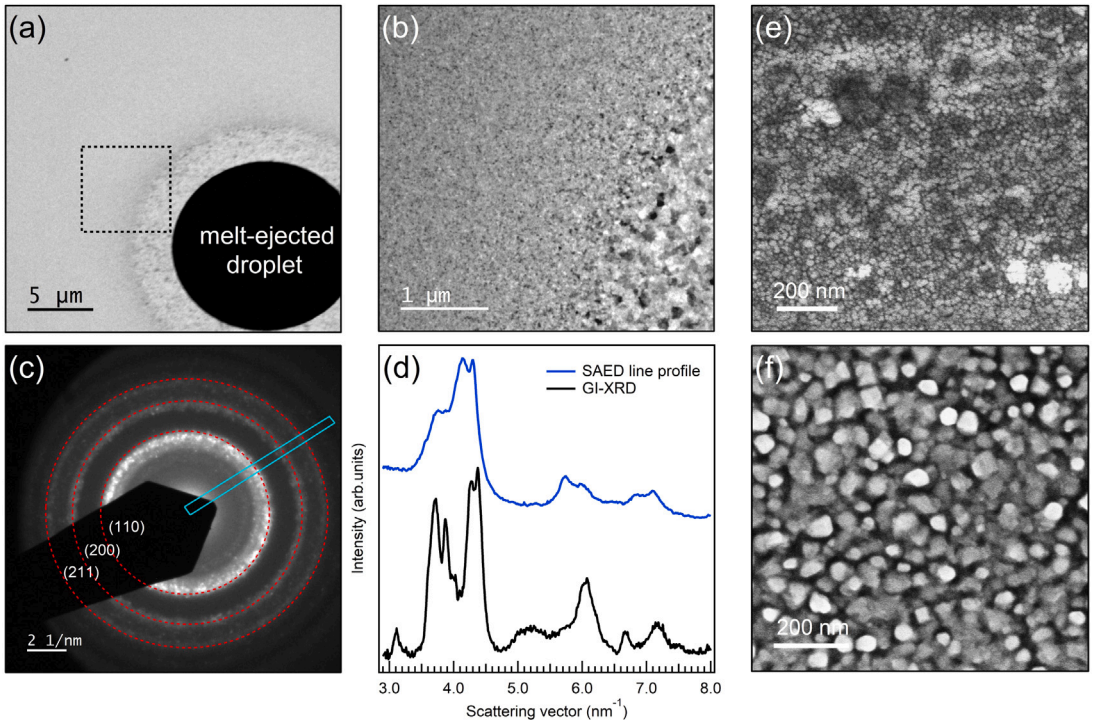

Fig. 3. Evolution of microstructure in a temperature gradient: (a) TEM analysis of an approximately 20 nm thick HfMoNbTiZr thin film deposited at 700 °C onto Si_3N_4 TEM windows, focused on a region close to an extraordinarily large melt droplet. (b) Zoomed-in TEM image of an area close to the droplet corresponding to the dashed black square in (a). The hot melt droplet leads to an increase in sample temperature upon impact, resulting in a temperature gradient from close to 700 °C to substantially higher (left to right in the image). The dark and bright spots are ascribed to crystallites with a diameter of up to 100 nm, which increase in size at increasing temperature. (c) SAED pattern of the region in (b) showing several continuous rings and bright diffraction spots. The expected diffraction rings for the pure BCC phase of the HEA are marked with red dashed circles. (d) Comparison between the integrated SAED line profile in panel (c) (light-blue curve) and a GI-XRD diffractogram of a HEA thin film deposited at 900 °C onto a Si_3N_4 substrate (black curve). (e–f) SEM images of air-exposed 100 nm thick HEA samples grown on Al_2O_3(0001) at RT (e), and at 900 °C (f). (For interpretation of the references to color in this figure legend, the reader is referred to the web version of this article.)

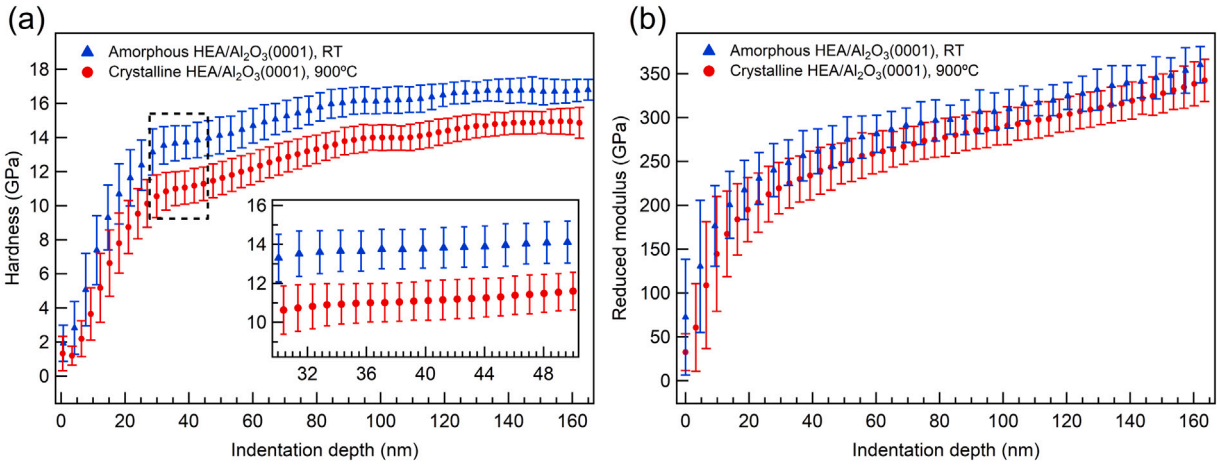

Fig. 4. (a) Hardness as a function of contact depth obtained from nanoindentation measurements of amorphous (blue curve, grown at room temperature) and crystalline (red curve, grown at 900 °C) HfMoNbTiZr thin films deposited onto Al_2O_3(0001). The thickness of both films was approximately 100 nm. The hardness values of the HEA/Al_2O_3(0001) system were extracted from the plateau region detected between approximately 30 nm and 50 nm of indentation depth (black dashed square), reported in the inset. (b) Corresponding reduced modulus as a function of contact depth obtained from the same nanoindentation measurements. (For interpretation of the references to color in this figure legend, the reader is referred to the web version of this article.)

The variation in the reduced modulus of the thin films (Fig. 4.b) and the PLD target (Figure S4.b) also reflects their different mechanical properties.

4. Discussion

The combined results of GI-XRD, TEM and EDX measurements clearly demonstrate that structural disorder in HfMoNbTiZr thin films of constant composition (within 1 at.%) is a tunable parameter that can be controlled independently of the composition via the growth conditions in pulsed laser deposition. In agreement with previous studies on metallic glasses grown with PLD [44], the temperature of the substrate is a key parameter. At low substrate temperatures, the HEA films are amorphous. The fully disordered phase is predominant up to substrate temperatures of at least 700 °C. Nanometer-sized crystallites embedded in the amorphous matrix give a subtle signal in the TEM

SAED pattern at 700 °C, but they do not present a signature in GI-XRD measurements, thus indicating low density, or extremely small particle sizes (in the range of 1–2 nm). The decrease in width of the amorphous halos and their shift towards higher diffraction angles with increasing temperature suggest the formation of a lower-energy amorphous structure and tunable packing density of the HEA films [50]. By increasing the substrate temperature to 800 °C, the crystallites grow in size and number, and are detected also with GI-XRD. However, the presence of high background signal in the region of the amorphous halos in the 800 °C diffractogram still indicates a significant level of disorder. After a further increase in growth temperature to 900 °C, the system overcomes the strongly disordered state and forms crystalline grains with high orientational preference. The high thermal energy required to induce crystallization is in agreement with temperature scales characteristic of refractory metals such as niobium, tantalum, and tungsten [51]. Here, this is borne out by a remarkably high temperature (between 800 °C and 900 °C) required to obtain sharp diffraction features, which are a clear indication of structural order over tens of nanometers. In comparison, the crystallization temperature of the majority of metalloid-free metallic glasses is in the range of ≈ 400–700 °C [51–53]. High crystallization temperatures are particularly desirable in industries such as energy production and space exploration, where coatings need to sustain highly corrosive and high temperature environments [51].

The crystalline HEA thin film exhibits a more complicated diffraction pattern than the bulk polycrystalline PLD target. The diffractograms of the films deposited onto sapphire at T = 800 °C and 900 °C show a combination of Debye–Scherrer rings, likely originating from the starting BCC-type polycrystalline phase, and several sharp diffraction spots stemming from a newly formed crystalline phase with well-defined orientation aligning with the $Al_2O_3(0001)$ substrate. The additional reflections at approximately 2θ = 29°, 41°, 51°, and 58° in Fig. 1.a are attributed to a primitive cubic structure (CsCl-type) with a lattice constant of approximately a = 3.12 Å. The decrease in the magnitude of the lattice constant in comparison to the original BCC structure of the PLD target is reflected in the shift of the reflections to larger 2θ values. The symmetry reduction to a primitive cubic cell manifests itself for example in the emergence of the (100) and (111) reflections at approximately 29° and 51°, respectively. This interpretation is supported by the recent report of a primitive cubic structure of the CsCl-type in HEAs containing refractory metals [54]. The stabilization of the CsCl-type crystal structure is ascribed to the difference in magnitude of the atomic radius between the larger Hf and Zr, on one side, and smaller Mo, Nb and Ti, on the other, which leads to a partial ordering of these two subgroups of atoms in two different crystallographic positions [54]. Therefore, in contrast to the arc-melted bulk target, which is close to the thermodynamically preferred structure, the out-of-equilibrium nature of PLD, with large variations in the local composition of crystalline nuclei, results in a polycrystalline structure of HfMoNbTiZr with two phases at the conditions tested here. This means that, technically, the crystalline layers of HfMoNbTiZr in this study are not single-phase solid solutions and therefore cannot be considered a 'true' HEA, in contrast to the PLD target.

The deposition of HfMoNbTiZr at 900 °C onto an amorphous Si_3N_4 layer further clarifies the mechanism of crystalline growth at high temperature. The amorphous structure of Si_3N_4 prevents the formation of a strong orientational preference in the film owing to its own lack of long-range order. The 2D-detector image corresponding to HfMoNbTiZr on Si_3N_4 (Fig. 1.f) shows the presence of continuous rings, whereas the one corresponding to HfMoNbTiZr on sapphire is characterized by bright spots at well-defined diffraction angles in three dimensions (Fig. 1.e). In contrast to the single-phase bulk target, the diffraction pattern of the film deposited on Si_3N_4 (Fig. 1.a) features multiple peak splittings. The majority of the new diffraction rings are close to the original reflection positions of the native BCC-type structure of the target, indicating the formation of various BCC intermetallic phases with similar lattice constants, estimated in the range between 3.2 Å and 3.8 Å. This is ascribed to a temperature-induced phase segregation of alloys with different compositions in the film. The peak at 29° is still present, providing further evidence for the existence of the cubic CsCl-type lattice discussed above. Interestingly, the orientational and structural preference provided by the $Al_2O_3(0001)$ substrate also strongly reduces the observed variation in lattice constants and is thus expected to improve the homogeneity of the layer.

Moreover, the continuous temperature variation observed in TEM measurements of a region close to a micrometer-sized droplet provides insight into the temperature-dependent variations in structure. The droplet is expected to substantially increase the local temperature of the film upon landing on the surface as a hot melt and slowly cooling down. As a consequence, a gradient in thermal energy is formed in the surroundings of the droplet, with decreasing temperature as one moves away from its boundary. In this region, the temperature is expected to be locally high enough (namely ≥ 900 °C) to induce the formation of large crystalline grains. The grain size decreases at larger distance from the droplet. The corresponding SAED line profile of Fig. 3.d shows the presence of several additional diffraction peaks, confirming temperature-induced formation of additional phases, most likely via phase separation. These results further clarify the growth mechanism of crystalline HfMoNbTiZr and confirm the formation of a layer with different coexisting phases at high temperature.

Nanoindentation measurements establish the important role that the thin-film structure plays in the mechanical properties of the coatings. As compared to conventional alloys and pure metals, many HEAs have been reported to be harder thanks to solid-solution strengthening and lattice distortion effects [19,55–57]. This is in line with our observation that the single-phase BCC crystal structure of the HfMoNbTiZr PLD target is harder than the corresponding individual pure metals Mo, Nb, Ti, Hf, Zr [58,59], in good agreement with previous reports on similar bulk high-entropy alloys [58,60–63]. Within the realm of HEAs, the relation of hardness and stoichiometry has been investigated across large compositional ranges [64–66], observing largely gradual variations with several percent of compositional change required to achieve a 10% change in the hardness. The small compositional variation (≤±1%) between the amorphous and crystalline HfMoNbTiZr is thus unlikely to be responsible for the clear change in hardness. The formation of a particular low-hardness phase at this specific composition can also be ruled out by the unremarkable variation between the individual nanoindentation points, which are expected to cover a small compositional range based on the broadening of XRD peaks at 900 °C, compared to the sharp diffraction peaks obtained for the PLD target. While the oxygen contents from EDX measurements are similar, an effect of oxygen impurities on the measured hardness values cannot be excluded.

The key difference of the two indented layers is their level of structural disorder. In the comparison of polycrystalline and amorphous HfMoNbTiZr, it must be stated that the values at the hardness plateau (11 GPa and 14 GPa) represent a convolution of the hardness of the alloy and the hard $Al_2O_3(0001)$ substrate. The difference between the hardness values of the polycrystalline and amorphous layers, however, can be directly related to the properties of the coatings, which were both grown on $Al_2O_3(0001)$ substrates and measured in an identical geometry. At the indentation depth of 30–50 nm, the enhancement of the hardness of the amorphous coating is clearest. At larger indentation depths, the measured hardness value rises continuously as more area is indenting the substrate. At the same time, the two indentation curves converge towards increasingly similar values. This slow collapse of the gap between the curves shows that the substrates have retained similar mechanical properties during the deposition of HfMoNbTiZr at different conditions. At the same time, the observed maximum in hardness difference at low indentation depths provides clear evidence that the amorphous HfMoNbTiZr film exhibits higher hardness than the crystalline HfMoNbTiZr film.

The difference between thin layers and the bulk target is likely also affected by the influence of the substrate on the measured values of the coatings. However, the interpretation that the HfMoNbTiZr layers are indeed harder than the bulk material is supported by reports of a reduced substrate influence for the case of coatings on substantially harder substrates. ("Substantially harder" refers to a factor of approximately 3 in hardness to keep the substrate contribution below 15% at an indentation depth of 30% of the layer thickness, respectively.) [67,68]. A quantitative comparison of the hardness values is hampered by the differences in surface roughness and indentation depth for the respective samples. For potential follow-up work focusing on the differences in the properties of bulk and thin-film HEAs, the use of the same indentation depths and polished bulk samples is recommended. The difference in hardness is likely also influenced by the difference in the microstructure between the bulk target grown using arc-melting and the pulsed-laser deposited layer with significantly smaller grains. An increase in hardness for thin-film samples can be expected to originate from grain-size thin-film effects, as described by the Hall-Petch relationship, which states that the hardness of nanomaterials increases with decreasing grain size. Down to a critical grain size of 10–30 nm, grain boundaries act as diffusion barriers hindering the propagation of dislocations [69]. In line with this interpretation, multi-phase HEA thin films commonly display increased hardness with respect to their single-phase counterparts [20,70,71]. Therefore, the coexistence of different crystalline phases is expected to play an important role in effectively impeding the motion of dislocations.

The increased hardness of amorphous HfMoNbTiZr is in agreement with the concept that metallic glasses are harder than crystalline alloys thanks to the lack of structural long-range order, which hinders the atoms' mobility and further enhances resistance to plastic deformations [2,36,72,73]. The microstructural differences observed using XRD, SEM, and TEM of the HEA layers grown at RT and high temperature agree with this picture. The absence of grains and extended defects in the amorphous layers formed at low temperature limits the propagation of strain. The formation of shear bands is likely to play an important role in the deformation, similar to the mechanisms reported for bulk metallic glasses [74,75]. Increasing temperature, on the other hand, enhances the level of order in the material, causing grains to nucleate and grow (see Fig. 3) and defects to be annihilated, which has previously been shown to lower the hardness of HEAs [76]. In the resulting polycrystalline films, plastic deformation can occur more easily, for example via dislocation glide and grain boundary sliding. Dislocations at the interface to the substrate, on the other hand, can form during indentation of both types of layers. However, simulations on amorphous alloy layers observe this effect only once the indenter is in close proximity to the interface [77].

Our results demonstrate that the targeted introduction of structural disorder to a (otherwise single-phase) HEA is a viable option for optimizing selected material properties. Increasing the level of disorder to first form a polycrystalline layer with different phases and then a fully amorphous film, raises the hardness of HfMoNbTiZr. The level of structural disorder represents an additional degree of freedom in the development of coatings, which has been effective to tune the optical, chemical and electronic properties of simple alloys without modifying their composition [44]. Here, this novel approach is extended to mechanical properties and high-entropy materials. Intentionally disordering a high-entropy alloy allows us to bridge the gap between the two seemingly different concepts of HEAs and HEMGs and customize the hardness of the material. This is for instance relevant to tune HEAs to fulfill either the requirements of mechanically stable, strong, and durable protective coatings against wear, stress, and fatigue or those of mechanical compliance of flexible electronics and wearable devices.

5. Conclusions

In summary, we demonstrate the growth of HfMoNbTiZr high-entropy alloy thin films with tunable level of structural disorder, ranging from fully amorphous to crystalline while maintaining an identical composition. This is achieved by appropriately varying the substrate temperature during pulsed laser deposition of the alloy. The amorphous phase exhibits remarkable thermal stability, being predominant up to a growth temperature of 700 °C. For complete crystallization, a higher temperature (900 °C) is required. Nanoindentation measurements highlight the intriguing mechanical properties of HfMoNbTiZr thin films, which display an increased hardness compared to the single-phase bulk PLD target. The hardness values measured for fully disordered, amorphous HfMoNbTiZr films on Al_2O_3(0001) further exceed those of the polycrystalline layers on the same substrate by approximately 30%. These results establish the importance of disorder as an effective parameter to tune the properties of materials without varying their composition, serving as a bridge between the different concepts of HEA and HEMG. Control over a gradual transition between order and disorder provides new versatility to materials design and has the potential to widen the scope of alloy coatings and enhance their individual performance.

CRediT authorship contribution statement

Alessandro Troglia: Formal analysis, Investigation, Visualization, Writing – original draft, Writing – review & editing. **Cyrian Leriche:** Formal analysis, Investigation, Writing – original draft. **Mike L. van de Poll:** Formal analysis, Investigation. **Christoph Morscher:** Formal analysis, Investigation. **Gert H. ten Brink:** Investigation, Methodology. **Bart J. Kooi:** Formal analysis, Investigation, Writing – review & editing. **Bart Weber:** Supervision, Writing – review & editing. **Roland Bliem:** Conceptualization, Supervision, Writing – review & editing.

Declaration of competing interest

The authors declare that they have no known competing financial interests or personal relationships that could have appeared to influence the work reported in this paper.

Data availability

Data will be made available on request.

Acknowledgments

We thank Dr. Sven Hennig for the support in the GI-XRD measurements and Dr. Anna Isaeva for valuable discussion of the structure measurements. This work has been carried out at the Advanced Research Center for Nanolithography (ARCNL), a public–private partnership between the University of Amsterdam (UvA), the Vrije Universiteit Amsterdam (VU), the Rijksuniversiteit Groningen (RUG), the Netherlands Organization for Scientific Research (NWO), and the semiconductor-equipment manufacturer ASML.

Appendix A. Supplementary data

Supplementary material related to this article can be found online at https://doi.org/10.1016/j.mtcomm.2024.110604.

References

[1] A.L. Greer, K.L. Rutherford, I.M. Hutchings, Wear resistance of amorphous alloys and related materials, Int. Mater. Rev. 47 (2) (2002) 87–112, http://dx.doi.org/10.1179/095066001225001067.

[2] A. Inoue, A. Takeuchi, Recent development and application products of bulk glassy alloys, Acta Mater. 59 (6) (2011) 2243–2267, http://dx.doi.org/10.1016/j.actamat.2010.11.027.

[3] A. Cai, G. Zhou, P. Li, D. Ding, Q. An, G. Zhou, Q. Yang, Y. Lin, H. Mao, Mechanical properties for a series of Zr-based bulk metallic glasses, J. Alloys Compd. 938 (2023) 168579, http://dx.doi.org/10.1016/j.jallcom.2022.168579.

[4] S. Madge, D. Louzguine-Luzgin, J. Lewandowski, A. Greer, Toughness, extrinsic effects and Poisson's ratio of bulk metallic glasses, Acta Mater. 60 (12) (2012) 4800–4809, http://dx.doi.org/10.1016/j.actamat.2012.05.025.

[5] A. Inoue, B. Shen, H. Koshiba, H. Kato, A.R. Yavari, Cobalt-based bulk glassy alloy with ultrahigh strength and soft magnetic properties, Nature Mater. 2 (10) (2003) 661–663, http://dx.doi.org/10.1038/nmat982.

[6] Z.P. Lu, C.T. Liu, J.R. Thompson, W.D. Porter, Structural amorphous steels, Phys. Rev. Lett. 92 (2004) 245503, http://dx.doi.org/10.1103/PhysRevLett.92.245503.

[7] J.J. Si, T. Wang, Y.D. Wu, Y.H. Cai, X.H. Chen, W.Y. Wang, Z.K. Liu, X.D. Hui, Cr-based bulk metallic glasses with ultrahigh hardness, Appl. Phys. Lett. 106 (25) (2015) 251905, http://dx.doi.org/10.1063/1.4923210.

[8] S. Moser, L. Moreschini, J. Jaćimović, O.S. Barišić, H. Berger, A. Magrez, Y.J. Chang, K.S. Kim, A. Bostwick, E. Rotenberg, L. Forró, M. Grioni, Tunable polaronic conduction in anatase TiO_2, Phys. Rev. Lett. 110 (2013) 196403, http://dx.doi.org/10.1103/PhysRevLett.110.196403.

[9] N. Portillo-Vélez, O. Olvera-Neria, I. Hernández-Pérez, A. Rubio-Ponce, Localized electronic states induced by oxygen vacancies on anatase TiO_2 (101) surface, Surf. Sci. 616 (2013) 115–119, http://dx.doi.org/10.1016/j.susc.2013.06.006.

[10] U. Diebold, The surface science of titanium dioxide, Surf. Sci. Rep. 48 (5) (2003) 53–229, http://dx.doi.org/10.1016/S0167-5729(02)00100-0.

[11] B. Gludovatz, A. Hohenwarter, D. Catoor, E.H. Chang, E.P. George, R.O. Ritchie, A fracture-resistant high-entropy alloy for cryogenic applications, Science 345 (6201) (2014) 1153–1158, http://dx.doi.org/10.1126/science.1254581.

[12] J.-W. Yeh, S.-K. Chen, S.-J. Lin, J.-Y. Gan, T.-S. Chin, T.-T. Shun, C.-H. Tsau, S.-Y. Chang, Nanostructured high-entropy alloys with multiple principal elements: Novel alloy design concepts and outcomes, Adv. Eng. Mater. 6 (5) (2004) 299–303, http://dx.doi.org/10.1002/adem.200300567.

[13] B. Cantor, I. Chang, P. Knight, A. Vincent, Microstructural development in equiatomic multicomponent alloys, Mater. Sci. Eng. A 375–377 (2004) 213–218, http://dx.doi.org/10.1016/j.msea.2003.10.257.

[14] L. Sun, R.J. Cava, High-entropy alloy superconductors: Status, opportunities, and challenges, Phys. Rev. Mater. 3 (2019) 090301, http://dx.doi.org/10.1103/PhysRevMaterials.3.090301.

[15] D. Miracle, O. Senkov, A critical review of high entropy alloys and related concepts, Acta Mater. 122 (2017) 448–511, http://dx.doi.org/10.1016/j.actamat.2016.08.081.

[16] E.P. George, D. Raabe, R.O. Ritchie, High-entropy alloys, Nat. Rev. Mater. 4 (2019) 515–534, http://dx.doi.org/10.1038/s41578-019-0121-4.

[17] Y. Ye, Q. Wang, J. Lu, C. Liu, Y. Yang, High-entropy alloy: challenges and prospects, Mater. Today 19 (6) (2016) 349–362, http://dx.doi.org/10.1016/j.mattod.2015.11.026.

[18] M.-H. Tsai, J.-W. Yeh, High-entropy alloys: A critical review, Mater. Res. Lett. 2 (3) (2014) 107–123, http://dx.doi.org/10.1080/21663831.2014.912690.

[19] N.I. Muhammad Nadzri, D.S.C. Halin, M.M. Al Bakri Abdullah, S. Joseph, M.A.A. Mohd Salleh, P. Vizureanu, D.-P. Burduhos-Nergis, A.V. Sandu, High-entropy alloy for thin film application: A review, Coatings 12 (12) (2022) 1842, http://dx.doi.org/10.3390/coatings12121842.

[20] K. Cui, Y. Zhang, High-entropy alloy films, Coatings 13 (3) (2023) 635, http://dx.doi.org/10.3390/coatings13030635.

[21] X.H. Yan, J.S. Li, W.R. Zhang, Y. Zhang, A brief review of high-entropy films, Mater. Chem. Phys. 210 (2018) 12–19, http://dx.doi.org/10.1016/j.matchemphys.2017.07.078, High-Entropy Materials.

[22] M.A. Tunes, V.M. Vishnyakov, Microstructural origins of the high mechanical damage tolerance of NbTaMoW refractory high-entropy alloy thin films, Mater. Des. 170 (2019) 107692, http://dx.doi.org/10.1016/j.matdes.2019.107692.

[23] R.K. Duchaniya, U. Pandel, P. Rao, Coatings based on high entropy alloys: An overview, Mater. Today: Proc. 44 (2021) 4467–4473, http://dx.doi.org/10.1016/j.matpr.2020.10.720.

[24] X. Feng, J. Zhang, Z. Xia, W. Fu, K. Wu, G. Liu, J. Sun, Stable nanocrystalline NbMoTaW high entropy alloy thin films with excellent mechanical and electrical properties, Mater. Lett. 210 (2018) 84–87, http://dx.doi.org/10.1016/j.matlet.2017.08.129.

[25] W. Xiong, A.X. Guo, S. Zhan, C.-T. Liu, S.C. Cao, Refractory high-entropy alloys: A focused review of preparation methods and properties, J. Mater. Sci. Technol. 142 (2023) 196–215, http://dx.doi.org/10.1016/j.jmst.2022.08.046.

[26] G.C. Gruber, A. Lassnig, S. Wurster, C. Gammer, M.J. Cordill, R. Franz, Tuning microstructure and properties of MoNbTaWZr high entropy alloy films by adjusting the parameters in high power impulse magnetron sputtering, Thin Solid Films 786 (2023) 140100, http://dx.doi.org/10.1016/j.tsf.2023.140100.

[27] G.C. Gruber, A. Lassnig, S. Zak, C. Gammer, M.J. Cordill, R. Franz, Thermal stability of MoNbTaTiW, MoNbTaVW and CrMoNbTaW thin films deposited by high power impulse magnetron sputtering, Surf. Coat. Technol. 454 (2023) 129189, http://dx.doi.org/10.1016/j.surfcoat.2022.129189.

[28] O. Senkov, J. Scott, S. Senkova, D. Miracle, C. Woodward, Microstructure and room temperature properties of a high-entropy TaNbHfZrTi alloy, J. Alloys Compd. 509 (20) (2011) 6043–6048, http://dx.doi.org/10.1016/j.jallcom.2011.02.171.

[29] N. Guo, L. Wang, L. Luo, X. Li, Y. Su, J. Guo, H. Fu, Microstructure and mechanical properties of refractory MoNbHfZrTi high-entropy alloy, Mater. Des. 81 (2015) 87–94, http://dx.doi.org/10.1016/j.matdes.2015.05.019.

[30] V. Pacheco, G. Lindwall, D. Karlsson, J. Cedervall, S. Fritze, G. Ek, P. Berastegui, M. Sahlberg, U. Jansson, Thermal stability of the HfNbTiVZr high-entropy alloy, Inorg. Chem. 58 (1) (2019) 811–820, http://dx.doi.org/10.1021/acs.inorgchem.8b02957.

[31] J. Kitagawa, K. Hoshi, Y. Kawasaki, R. Koga, Y. Mizuguchi, T. Nishizaki, Superconductivity and hardness of the equiatomic high-entropy alloy HfMoNbTiZr, J. Alloys Compd. 924 (2022) 166473, http://dx.doi.org/10.1016/j.jallcom.2022.166473.

[32] R.N. Elshaer, S. El-Hadad, A. Nofal, Influence of heat treatment processes on microstructure evolution, tensile and tribological properties of Ti6Al4V alloy, Sci. Rep. 13 (2023) 11292, http://dx.doi.org/10.1038/s41598-023-38250-2.

[33] Y. Xu, L. Jeurgens, L. Lin, S. Ma, S. Zhu, Y. Huang, Y. Liu, J. Qiao, Z. Wang, Revealing the univariate effect of structural order on the oxidation of ternary alloys: Amorphous vs. crystalline Cu–Zr–Al alloys, Corros. Sci. 183 (2021) 109309, http://dx.doi.org/10.1016/j.corsci.2021.109309.

[34] R.C. Munoz, C. Arenas, Size effects and charge transport in metals: Quantum theory of the resistivity of nanometric metallic structures arising from electron scattering by grain boundaries and by rough surfaces, Appl. Phys. Rev. 4 (1) (2017) 011102, http://dx.doi.org/10.1063/1.4974032.

[35] J.P. Chu, J. Jang, J. Huang, H. Chou, Y. Yang, J. Ye, Y. Wang, J. Lee, F. Liu, P. Liaw, Y. Chen, C. Lee, C. Li, C. Rullyani, Thin film metallic glasses: Unique properties and potential applications, Thin Solid Films 520 (16) (2012) 5097–5122, http://dx.doi.org/10.1016/j.tsf.2012.03.092.

[36] S. Alvi, M. Milczarek, D.M. Jarzabek, D. Hedman, M.G. Kohan, N. Levintant-Zayonts, A. Vomiero, F. Akhtar, Enhanced mechanical, thermal and electrical properties of high-entropy HfMoNbTaTiVWZr thin film metallic glass and its nitrides, Adv. Eng. Mater. 24 (9) (2022) 2101626, http://dx.doi.org/10.1002/adem.202101626.

[37] S. Zhao, H. Wang, L. Xiao, N. Guo, D. Zhao, K. Yao, N. Chen, High strain rate sensitivity of hardness in quinary Ti-Zr-Hf-Cu-Ni high entropy metallic glass thin films, Phys. E: Low-Dimens. Syst. Nanostruct. 94 (2017) 100–105, http://dx.doi.org/10.1016/j.physe.2017.07.021.

[38] M. Tunes, H. Vo, J. Baldwin, T. Saleh, S. Fensin, O. El-Atwani, Perspectives on novel refractory amorphous high-entropy alloys in extreme environments, Appl. Mater. Today 32 (2023) 101796, http://dx.doi.org/10.1016/j.apmt.2023.101796.

[39] P.L. Wei Li, P.K. Liaw, Microstructures and properties of high-entropy alloy films and coatings: a review, Mater. Res. Lett. 6 (4) (2018) 199–229, http://dx.doi.org/10.1080/21663831.2018.1434248.

[40] N. Tüten, D. Canadinc, A. Motallebzadeh, B. Bal, Microstructure and tribological properties of TiTaHfNbZr high entropy alloy coatings deposited on Ti-6Al-4V substrates, Intermetallics 105 (2019) 99–106, http://dx.doi.org/10.1016/j.intermet.2018.11.015.

[41] X. Liu, W. Cai, Y. Zhang, L. Wang, J. Wang, Tuning microstructure and mechanical and wear resistance of ZrNbTiMo refractory high-entropy alloy films via sputtering power, Front. Mater. 10 (2023) 1145631, http://dx.doi.org/10.3389/fmats.2023.1145631.

[42] X. Chang, M. Zeng, K. Liu, L. Fu, Phase engineering of high-entropy alloys, Adv. Mater. 32 (14) (2020) 1907226, http://dx.doi.org/10.1002/adma.201907226.

[43] N. Saunders, A.P. Miodownik, Phase formation in co-deposited metallic alloy thin films, J. Mater. Sci. 22 (1987) 629–637, http://dx.doi.org/10.1007/BF01160780.

[44] A. Troglia, V. Vollema, S. Cassanelli, E. van Heumen, J. van de Groep, A. de Visser, R. Bliem, Tuning material properties via disorder: From crystalline alloy to metallic glass, Mater. Today Phys. 29 (2022) 100893, http://dx.doi.org/10.1016/j.mtphys.2022.100893.

[45] W.C. Oliver, G.M. Pharr, Measurement of hardness and elastic modulus by instrumented indentation: Advances in understanding and refinements to methodology, J. Mater. Res. 19 (2004) 3–20, http://dx.doi.org/10.1557/jmr.2004.19.1.3.

[46] N.S. Gingrich, The diffraction of X-rays by liquid elements, Rev. Modern Phys. 15 (1943) 90–110, http://dx.doi.org/10.1103/RevModPhys.15.90.

[47] G. Yetik, A. Troglia, S. Farokhipoor, S. van Vliet, J. Momand, B.J. Kooi, R. Bliem, J.W. Frenken, Ultrathin, sputter-deposited, amorphous alloy films of ruthenium and molybdenum, Surf. Coat. Technol. 445 (2022) 128729, http://dx.doi.org/10.1016/j.surfcoat.2022.128729.

[48] S. Fähler, K. Sturm, H.-U. Krebs, Resputtering during the growth of pulsed-laser-deposited metallic films in vacuum and in an ambient gas, Appl. Phys. Lett. 75 (24) (1999) 3766–3768, http://dx.doi.org/10.1063/1.125449.

[49] K. Sturm, S. Fähler, H.-U. Krebs, Pulsed laser deposition of metals in low pressure inert gas, Appl. Surf. Sci. 154–155 (2000) 462–466, http://dx.doi.org/10.1016/S0169-4332(99)00407-9.

[50] H. Luan, X. Zhang, H. Ding, F. Zhang, J.H. Luan, Z.B. Jiao, Y.-C. Yang, H. Bu, R. Wang, J. Gu, C. Shao, Q. Yu, Y. Shao, Q. Zeng, N. Chen, C.T. Liu, K.-F. Yao, High-entropy induced a glass-to-glass transition in a metallic glass, Nature Commun. 13 (2004) 2183, http://dx.doi.org/10.1038/s41467-022-29789-1.

[51] J. Howard, K. Carlson, D. Chidambaram, High-temperature metallic glasses: Status, needs, and opportunities, Phys. Rev. Mater. 5 (2021) 040301, http://dx.doi.org/10.1103/PhysRevMaterials.5.040301.

[52] D.V. Louzguine-Luzgin, D.B. Miracle, L. Louzguina-Luzgina, A. Inoue, Comparative analysis of glass-formation in binary, ternary, and multicomponent alloys, J. Appl. Phys. 108 (10) (2010) 103511, http://dx.doi.org/10.1063/1.3506687.

[53] C. Suryanarayana, A. Inoue, Iron-based bulk metallic glasses, Int. Mater. Rev. 58 (3) (2013) 131–166, http://dx.doi.org/10.1179/1743280412Y.0000000007.

[54] K. Stolze, J. Tao, F.O. von Rohr, T. Kong, R.J. Cava, Sc–Zr–Nb–Rh–Pd and Sc–Zr–Nb–Ta–Rh–Pd high-entropy alloy superconductors on a CsCl-type lattice, Chem. Mater. 30 (3) (2018) 906–914, http://dx.doi.org/10.1021/acs.chemmater.7b04578.

[55] P. Edalati, A. Mohammadi, M. Ketabchi, K. Edalati, Ultrahigh hardness in nanostructured dual-phase high-entropy alloy AlCrFeCoNiNb developed by high-pressure torsion, J. Alloys Compd. 884 (2021) 161101, http://dx.doi.org/10.1016/j.jallcom.2021.161101.

[56] E. George, W. Curtin, C. Tasan, High entropy alloys: A focused review of mechanical properties and deformation mechanisms, Acta Mater. 188 (2020) 435–474, http://dx.doi.org/10.1016/j.actamat.2019.12.015.

[57] G.C. Gruber, A. Lassnig, S. Zak, C. Gammer, M.J. Cordill, R. Franz, Synthesis and structure of refractory high entropy alloy thin films based on the MoNbTaW system, Surf. Coat. Technol. 439 (2022) 128446, http://dx.doi.org/10.1016/j.surfcoat.2022.128446.

[58] H. Yao, J. Qiao, J. Hawk, H. Zhou, M. Chen, M. Gao, Mechanical properties of refractory high-entropy alloys: Experiments and modeling, J. Alloys Compd. 696 (2017) 1139–1150, http://dx.doi.org/10.1016/j.jallcom.2016.11.188.

[59] G.V. Samsonov, Handbook of the Physicochemical Properties of the Elements, Springer US, 1968, pp. 387–446, http://dx.doi.org/10.1007/978-1-4684-6066-7_7, Ch. Mechanical Properties of the Elements.

[60] M. Srikanth, A.R. Annamalai, A. Muthuchamy, C.-P. Jen, A review of the latest developments in the field of refractory high-entropy alloys, Crystals 11 (6) (2021) 612, http://dx.doi.org/10.3390/cryst11060612.

[61] F. Liu, P.K. Liaw, Y. Zhang, Recent progress with BCC-structured high-entropy alloys, Metals 12 (3) (2022) 501, http://dx.doi.org/10.3390/met12030501.

[62] F. Tian, L.K. Varga, N. Chen, J. Shen, L. Vitos, Empirical design of single phase high-entropy alloys with high hardness, Intermetallics 58 (2015) 1–6, http://dx.doi.org/10.1016/j.intermet.2014.10.010.

[63] S. Maiti, W. Steurer, Structural-disorder and its effect on mechanical properties in single-phase TaNbHfZr high-entropy alloy, Acta Mater. 106 (2016) 87–97, http://dx.doi.org/10.1016/j.actamat.2016.01.018.

[64] P. Wilson, R. Field, M. Kaufman, The use of diffusion multiples to examine the compositional dependence of phase stability and hardness of the Co-Cr-Fe-Mn-Ni high entropy alloy system, Intermetallics 75 (2016) 15–24, http://dx.doi.org/10.1016/j.intermet.2016.04.007.

[65] Y.-J. Chang, C.-Y. Jui, W.-J. Lee, A.-C. Yeh, Prediction of the composition and hardness of high-entropy alloys by machine learning, JOM 71 (2019) 3433–3442, http://dx.doi.org/10.1007/s11837-019-03704-4.

[66] P. Nagy, N. Rohbeck, Z. Hegedűs, J. Michler, L. Pethö, J.L. Lábár, J. Gubicza, Microstructure, hardness, and elastic modulus of a multibeam-sputtered nanocrystalline Co-Cr-Fe-Ni compositional complex alloy film, Materials 14 (12) (2021) 3357, http://dx.doi.org/10.3390/ma14123357.

[67] H. Pelletier, J. Krier, P. Mille, Characterization of mechanical properties of thin films using nanoindentation test, Mech. Mater. 38 (12) (2006) 1182–1198, http://dx.doi.org/10.1016/j.mechmat.2006.02.011.

[68] A. Bhattacharya, W. Nix, Analysis of elastic and plastic deformation associated with indentation testing of thin films on substrates, Int. J. Solids Struct. 24 (12) (1988) 1287–1298, http://dx.doi.org/10.1016/0020-7683(88)90091-1.

[69] I. Ovid'ko, R. Valiev, Y. Zhu, Review on superior strength and enhanced ductility of metallic nanomaterials, Prog. Mater. Sci. 94 (2018) 462–540, http://dx.doi.org/10.1016/j.pmatsci.2018.02.002.

[70] L. Lin, X. Xian, Z. Zhong, C. Chen, Z. Zhu, Y. Wu, P.K. Liaw, A multi-phase $CrMnFeCoNiAl_{0.75}$ high-entropy alloy with high strength at intermediate temperature, Intermetallics 120 (2020) 106744, http://dx.doi.org/10.1016/j.intermet.2020.106744.

[71] S. Fritze, C.M. Koller, L. von Fieandt, P. Malinovskis, K. Johansson, E. Lewin, P.H. Mayrhofer, U. Jansson, Influence of deposition temperature on the phase evolution of HfNbTiVZr high-entropy thin films, Materials 12 (4) (2019) 587, http://dx.doi.org/10.3390/ma12040587.

[72] D.V. Louzguine-Luzgin, A. Inoue, Bulk metallic glasses: Formation, structure, properties, and applications, in: K. Buschow (Ed.), in: Handbook of Magnetic Materials, vol. 21, Elsevier, 2013, pp. 131–171, http://dx.doi.org/10.1016/B978-0-444-59593-5.00003-9, Ch. 3.

[73] S. Sarker, R. Tang-Kong, R. Schoeppner, L. Ward, N.A. Hasan, D.G. Van Campen, I. Takeuchi, J. Hattrick-Simpers, A. Zakutayev, C.E. Packard, A. Mehta, Discovering exceptionally hard and wear-resistant metallic glasses by combining machine-learning with high throughput experimentation, Appl. Phys. Rev. 9 (1) (2022) 011403, http://dx.doi.org/10.1063/5.0068207.

[74] W.J. Wright, R. Saha, W.D. Nix, Deformation mechanisms of the $Zr_{40}Ti_{14}Ni_{10}Cu_{12}Be_{24}$ bulk metallic glass, Mater. Trans. 42 (4) (2001) 642–649, http://dx.doi.org/10.2320/matertrans.42.642.

[75] C. Schuh, T. Nieh, A nanoindentation study of serrated flow in bulk metallic glasses, Acta Mater. 51 (1) (2003) 87–99, http://dx.doi.org/10.1016/S1359-6454(02)00303-8.

[76] A. Xia, R. Franz, Thermal stability of MoNbTaVW high entropy alloy thin films, Coatings 10 (10) (2020) 941, http://dx.doi.org/10.3390/coatings10100941.

[77] K.E. Avila, V.H. Vardanyan, S. Küchemann, H.M. Urbassek, Response of an amorphous/crystalline interface to nanoindentation: an atomistic study, Appl. Surf. Sci. 551 (2021) 149285, http://dx.doi.org/10.1016/j.apsusc.2021.149285.